Journal of Thermal Analysis and Calorimetry
An International Forum for Thermal Studies

https://www.springer.com/journal/10973

IMPACT FACTOR = 4.626

Accepted November 10th 2021

COMPUTATION OF VON KARMAN THERMO-SOLUTAL SWIRLING FLOW OF A NANOFLUID OVER A ROTATING DISK TO A NON-DARCIAN POROUS MEDIUM WITH HYDRODYNAMIC/THERMAL SLIP

J.C. Umavathi

Professor, Department of Mathematics, Gulbarga University Gulbarga -585106, Karnataka,

India. **Email: drumavathi@rediffmail.com**

O. Anwar Bég

Professor, Department of Aeronautical/Mechanical Engineering, School of Science, Engineering and Environment (SEE), University of Salford, Newton Building, Manchester, M5 4WT, ***UK.***

Email: O.A.Beg@salford.ac.uk

ABSTRACT:

Motivated by recent trends in spin coating operations in chemical engineering which are exploiting nanomaterials, the present article investigates theoretically and numerically the steady mass and heat transfer in Von Karman swirling slip flow of a nanofluid from a rotating disk touching to a homogenous non-Darcy porous medium. The porous medium is simulated with a *Darcy-Forchheimer-Brinkman model*. To track the thermophoresis and Brownian movement of the nanoparticles the Buongiorno nanoscale model is used. Von Karman similarity variables are deployed to transform the partial differential conservation equations into a system of highly coupled, nonlinear, dimensionless ordinary differential equations (ODE's). These similarity boundary layer equations i. e. continuity, momentum, energy and nanoparticle concentration (volume fraction) are solved with bvp4c shooting quadrature in MATLAB. Validation with earlier studies is included. Further verification with an Adams-Moulton predictor-corrector method is conducted. The influence of *velocity (momentum) slip coefficient*, *thermal slip*, *Darcian bulk drag parameter (inverse permeability)*, *Forchheimer inertial parameter*, *Browninan motion parameterm Schmidt number*, *thermophoresis parameter and Prandtl number* on *radial, tangential (azimuthal) and axial velocity components, temperature and nanoparticle concentration* are visualized graphically. The distributions for skin friction component and Nusselt number are also computed. Radial, axial and tangential velocities are reduced with increasing Forchheimer inertial drag and hydrodynamic wall slip whereas they are elevated with increasing permeability (decreasing inverse Darcy parameter). Thermal and nanoparticle concentration boundary layers are also markedly modified with an increment in Forchheimer

inertial parameter, Schmidt number, Prandtl number, thermophoresis and Brownian motion parameters.

KEYWORDS: *Rotating disk, Porous medium, Inertial drag, Nanofluid, Buongiorno model, MATLAB; Adams-Moulton predictor-corrector method; Von Karman swirling flow; Spin coating dynamics.*

NOMENCLATURE

Roman

C	Local nanoparticle concentration (moles/m^3)
C_f	Skin friction coefficient (-)
C_∞	Ambient nanoparticle concentration (moles/m^3)
D_B	Brownian diffusion coefficient (-)
D_T	Thermophoretic diffusion coefficient (-)
Nb	Brownian motion parameter (-)
Nt	Thermophoresis parameter (-)
$f(\eta),\ g(\eta)$	Dimensionless velocity components (-)
I	Inertial (Forchheimer) porous medium drag parameter (-)
k	Thermal conductivity (W/mK)
L_1	Hydrodynamic slip coefficient (-)
L_2	Thermal slip (jump) coefficient (-)
Nu_r	Local Nusselt number (-)
p	Nanofluid pressure (Pa)
Pr	Prandtl number (-)
Re	Rotational Reynolds number (-)
$(r,\ \varphi,\ z)$	Cylindrical coordinate system (m)
Sc	Schmidt number (-)
T	Local nanofluid temperature (K)
T_w	Constant disk temperature (K)
T_∞	Ambient fluid temperature (K)

(u, v, w) Velocity components along (r, φ, z) directions

Greek Symbols

τ Ratio of effective heat capacity of the nanoparticle material to base fluid

σ Inverse permeability parameter (-)

η Similarity variable (-)

α_f Thermal diffusivity of base fluid (m^2/s)

ν_f Kinematic viscosity (m^2/s)

κ Permeability of porous medium (m^2)

γ Dimensionless velocity (hydrodynamic) slip coefficient (-)

α Dimensionless thermal slip coefficient (-)

Ω Angular velocity of rotating disk (rad/s)

ρ_f Fluid density (kg/m^3)

τ_r, τ_θ Radial and tangential wall stresses (N/m^2)

θ Dimensionless temperature (-)

ϕ Dimensionless nanoparticle concentration (-)

Superscripts

' Differentiation w r t η

1. INTRODUCTION

Viscous flows from a rotating disk emerge in many intriguing applications in industry including spin coating deposition, food processing, chemical mixing, turbomachinery, heat exchangers, computer disk drive cooling, lubrication and membrane oxygenators. Von Karman [1] initiated the analysis of rotating disk flows in 1921 by considering three-dimensional viscous flow over an infinite rotating disk having a constant angular velocity, in which he introduced the famous Von Karman similarity transformations. Later, Wagner [2] extended the Von Karman problem for an infinite rotating disk with steady motion of incompressible viscous fluid to consider convective heat transfer. Further analysis on thermal aspects of Von Karman swirl flow was conducted by Cobb and Saunders [3]. Millsaps and Pohlhausen [4] considered Von Karman swirling flow with heat transfer and viscous dissipation. Kobayashi *et al.* [5] extended the laminar simulations

reported earlier to consider transitional and turbulent flow with the generation of spiral vortex patterns, elucidating the interplay between both the centrifugal and Coriolis forces in swirling disk flow. Awad [6] presented asymptotic solutions for thermal convection in swirling disk flow at very low and very high Prandtl numbers, computing Nusselt numbers for these extreme scenarios. Mass (species) diffusion and rheological effects were explored by Grief and Paterson [7] and later Mishra and Singh [8] for rotating disk flow. He *et al.* [9] measured the effect of disk rotating speed in Von Karman thermosolutal flow. Rashaida *et al.* [10] evaluated theoretically the rate of mass transfer using Bingham fluid over a rotating disk. More recently, motivated by emerging technologies in chemical, civil, biomedical and aerospace engineering, researchers have further extended the laminar Von Karman swirl problem to consider many complex multi-physics aspects including magnetohydrodynamics e.g. Turkyilmazoglu [11], radiative heat transfer and wall transpiration e.g. Bég *et al.* [12], electrokinetic ionic fluids e. g. Shuaib et al. [13] thermodynamic optimization and disk stretching e.g. Bég *et al.* [14] variable disk thickness with pseudoplastic/dilatant fluid behaviour e.g. Xun *et al.* [15] non-Fourier thermal conduction effects in dual disk systems e.g. Mishra *et al.* [16] and proton-effective rotating disc photocatalytic reactor swirl flow for environmental systems with chemical kinetics e.g. Zhang *et al.* [17].

The thermal properties of working liquids are of critical importance for optimizing engineering performance. To achieve enhancement in for example thermal conductivity of liquids, many researchers have explored a variety of possible mechanisms. Nanotechnology in particular has produced exceptional progress in this regard via the robust development of ultrafine-performance heat transfer liquids which have been termed *nanofluids*. Nanofluids are combinations of solid nanometer sized *metallic or non-metallic* (carbon-based) particles which are less than 100nm in size. For heat transfer processes, popular metallic nano-sized particles include alumina, copper, gold, silver, zinc, iron, molybdenum, titanium and relevant base liquids are water, oil, ethylene glycol, etc. Many studies of micro/nanofluid transport phenomena have been communicated in recent years. The Influence of variable viscosity, thermal conductivity, velocity and thermal slip effects on a steady two-dimensional magnetohydrodynamic micropolar fluid over a stretching sheet was numerically by analyzed by Rahman *et al.* [18]. They came to the conclusion that astronger transverse magnetic field decelerates the flow and elevates the temperature. Also

increasing viscosity parameter and hydrodynamic slip accelerates the flow further from the plate surface. Khan *et al.* [19] addressed the steady three-dimensional flow of an Oldroyd-B nanofluid over a bidirectional stretching surface with heat generation/absorption effects, noting that increasing values of the Brownian motion parameter and thermophoresis parameter leads to an increase in the temperature field and thermal boundary layer thickness while the opposite behavior is observed for concentration field and concentration boundary layer thickness. The heat and mass transfer characteristics of three-dimensional steady flow of Burgers nanofluid over a bidirectional stretching surface was studied by Khan *et al.* [20]. They observed that for enlarging values of the Brownian motion parameter lead to an attenuation in the nanoparticle concentration field as well as the concentration boundary layer thickness. Likewise, it was also noticed that the concentration magnitudes are suppressed with Deborah number in comparison to Brownian motion parameter. Masood *et al.* [21] analysed the magnetohydrodynamic boundary layer flow of power-law nanofluid over a non-linear stretching sheet, showing that velocity decreases with increasing stretching parameter. Khan *et al.* [22] analyzed the two-dimensional boundary layer flow of Burgers' nanofluid over a stretching surface, showing that Deborah number (viscoelastic parameter) has opposite effects on temperature and mass fraction function Generalized Burgers nanofluid flow from a stretching sheet in the presence of heterogeneous-homogeneous chemical reactions was addressed by Khan *et al.* [23]. Unsteady three-dimensional flow of Eyring-Powell nanofluid under convective and nanoparticles mass flux conditions was made by Khan *et al.* [24]. Metallic-based nanofluids have often been examined in these studies. They often are biocompatible and therefore of considerable interest in green industrial and biomedical systems including wound treatment, cancer therapy, nano-pharmacodynamics (drug delivery), nano-enhanced rotating membrane bioreactors (Beg *et al.* [25]) etc. Nanofluids were introduced by American energy engineer, Stephen Choi [26] originally to develop coolants for automotive applications without incurring agglomeration and sedimentation effects experienced with larger (micron-sized) particles. Eastman *et al*. [27] demonstrated that nanoparticles can enhance thermal conductivity by 40% by doping with 1% nanoparticles (copper) in oil or ethylene glycol. Subsequently a considerable effort has been made by numerous researchers to investigate increasingly diverse applications of nanofluids owing to their superior properties i.e. large thermal conductivity, long-term stability and minimal obstructive effects in flow passages.

These studies have largely been theoretical and computational in nature and provide an important compliment to experimental investigations. Of particular relevance to swirling flow applications, are *rotating nanofluid models*. These incorporate Coriolis body force effects in addition to species diffusion (nanoparticle mass transfer) and other physical effects (heat transfer, time-dependence, viscous dissipation, thermal stratification, chemical reactions etc). Interesting computational studies of rotating nanofluid dynamics include Rana *et al.* [28] who investigated Richardson and Taylor number effects on transient rotating hydromagnetic nanofluid stretching sheet flow in polymer processing. Thumma *et al.* [29] used a variational finite element technique to compute thermo-solutal magneto-convection from a spinning vertical surface with viscous heating effects. Yadav *et al.* [30] simulated the hydromagnetic stability of rotating nanofluids using linear stability theory and a Galerkin finite element technique for several scenarios. Rotating disk swirling flows of nanofluids have also received some attention. Bachok *et al.* [31] employed Kelelr's implicit box method to numerically analyze the relative performance of two different nanofluid effective thermal conductivity models (Maxwell–Garnett model and Patel model) for laminar flow over a permeable rotating disk with wall suction and injection effects. Mahanthesh *et al.* [32] computed numerically the swirling flow of Ti_6Al_4V or *AA*7072 -water nanofluids over a rotating disk with heat flux and heat source conditions, considering also shape effects for different nanoparticles (laminates, tubes, spheres, tetrahedrons and hexahedrons). Makinde *et al.* [33] simulated the impact of radiative flux on swirling magnetohydrodynamic aluminum/titanium-water nanofluid flow from a rotating disk. They also considered Ohmic and viscous heating noting that titanium alloy nanoparticles achieve superior thermal performance compared with aluminium alloy nanoparticles. Sheikholeslami *et al.* [34] computed the steady nanofluid deposition on an inclined rotating disk with a fourth order Runge–Kutta method, noting that Nusselt number is elevated with normalized thickness, Schmidt number, Brownian parameter and thermophoretic parameter and furthermore that Schmidt number, Brownian parameter and thermophoretic parameter are directly proportional to latent heat whereas normalized thickness exhibits an inverse relationship. Further studies of swirling flows of nanofluids include Hayat *et al.* [35] (on homogeneous-heterogeneous reactions in Iron oxide magnetite-water nanofluids), Yin *et al.* [36] (radial linear stretching disk nanofluid flow) and Mushtaq *et al.* [37] (rotating exponentially stretching sheet nanofluid transport).

Many other studies of nanofluid convection flows have been reported using the Buongiorno model. Khan *et al.* [38] explored the impact of nonlinear thermal radiation and variable thermal conductivity on Cross rheological nanofluid flow. It was observed that the thermophoresis and Brownian motion mechanisms significantly affected heat transport. Khan *et al.* [39] focused on the characteristics of heat sink-source and melting in time-dependent Falkner–Skan flow of Cross nanofluid. They noted that velocity of the Cross nanoliquid is boosted with larger melting and velocity ratio parameters and increment in Schmidt number produced a boost in concentrations. The hydromagnetic flow of Sisko nanofluid along an unsteady curved surface with non-uniform heat source/sink was addressed by Khan *et al.* [40], who showed that greater magnetic parameter accelerates the flow and increment in thermophoresis parameter elevates the nanoparticle concentration. Khan *et al*. [41] scrutinized the reactive magnetized Cross nanofluid flow external to a cylindrical surface. Their results revealed that temperature is elevated with larger thermophoretic parameter whereas nanoparticle concentration is depleted with greater activation energy parameter. Further studies include Khan *et al.* [42] who examined the effects of Brownian motion and thermophoresis on time-dependent magnetic non-Newtonian (Sisko) nanofluid flow from a curved stretching surface. They observed that nanoparticle concentration is intensified with greater thermophoresis parameter and velocity is enhanced by augmenting the values of curvature parameter. Khan *et al.* [43] also developed a nonlinear mathematical model for Williamson rheological nanofluid fluid along a convectively heated moving surface. They showed that the temperature is elevated with larger Brownian movement and thermophoretic parameters. Variable characteristics of viscosity and thermal conductivity in peristaltic flow of magneto-Carreau nanoliquid with heat transfer irreversibility was studied by Khan *et al.* [44]. Khan *et al.* [45] also analyzed the peristaltic pumping of aqueous nanofluids containing SWCNTs and MWCNT's with entropy optimization in a non-uniform channel.

In many practical engineering operations, *porous media* may be deployed to exploit their excellent flow control and filtration properties. The most popular methodology for simulating porous media hydrodynamic effects is the classical Darcy model [46] which established experimentally the phenomenological relation through the pressure drop across a saturated porous medium and the flow rate and features permeability (hydraulic conductivity) of the porous medium. It also assumes isotropic and homogenous properties. Porous media have

therefore been explored extensively in mathematical models of industrial processes and notable examples in this regard are Prasad and Kulacki [47], Vasseur *et al.* [48]. More recently a diverse spectrum of thermal boundary conditions, thermophysical effects and numerical techniques have been described by Umavathi *et al.* [49, 50, 51, 52] for vertical duct porous media transport problems. These studies have utilized the Darcian model which provides an accurate simulation for low velocity transport. For higher velocity flows or those featuring vorticity diffusion at the boundaries, which may be encountered in for example high-speed coating processes or medical devices, the Darcy model is inadequate and needs to be modified to simulate inertial porous medium effects, viscous effects etc. Two notable modifications of Darcy's law which have been developed to examine nonlinear fluid dynamic effects are the Brinkman [53] and Forchheimer [54] extensions, which account for the viscous stresses with the bounding walls and the non-linear (second order inertial) drag effect over the solid matrix, respectively. The Darcy-Forchheimer drag model for example can simulate flows quite accurately up to Reynolds numbers of about 100, after which chaotic and subsequently disturbed flow regimes arise. A more general approach is the Brinkman-extended Darcy-Forchhemer model which is a more robust non-Darcy model, and which neatly fits into the framework of the Navier-Stokes viscous flow model. This approach has received considerable attention in recent years in chemical and mechanical engineering. Interesting studies in this regard include Umavathi and Bég [55] (on thermosolutal reactive convective non-Darcy flow in a vertical channel with boundary conditions of the third kind), Rawat *et al.* [56] (on unsteady electroconductive microstructural convective flow under buoyancy forces with heat generation), Subba Rao *et al.* [57] (on thermosolutal nanofluid coating flow of a cylindrical pipe in non-Darcy porous media), Bég *et al.* [58] (on geothermal radiative-convective flow from a curved body in non-Darcy saturated permeable media) and Bég *et al.* [59] (on buoyancy-driven two-phase blood flow pumping in a hemodynamic purification device). Bég *et al.* [60] generalized the Darcy model to anisotropic permeability and Forchheimer drag effects for spin coating of a cone with mass diffusion in porous media using Adomian decomposition, generalized differential quadrature and shooting quadrature. Rotating disk flow to non-Newtonian saturated non-Darcy porous media was investigated by Bég *et al.* [61] who deployed MATLAB quadrature and finite element methods to compute radial, tangential and axial velocity distributions in pseudoplastic/dilatant

biopolymeric coating flows with the Brinkman-Darcy-Forcheimmer model. They noted the significant damping effect on all velocity components associated with stronger Forchheimer inertial parameter.

The above studies generally assumed the *classical no-slip wall condition*. However, in nanomaterial coating and other complex deposition operations, *wall slip effects* are known to exist. Alternatively, a Knudsen number may be deployed which relates the mean free path of molecules to a characteristic length. A critical parameter for stable coating synthesis is the also the disk rotation speed. Optimized coatings can be produced by balancing the correct parameters to achieve more homogenous film distribution over a rotating disk. Smart nanofluid coatings are increasingly being deployed for corrosion protection in aerospace engineering and ultra-thin membranes for sensor applications. Computational studies of slip dynamics in rheological and nanofluids have also received some interest in recent years and have considered both external coating and internal flows. Presentative studies in coating systems include Prasad *et al.* [62] (on Casson viscoplastic axisymmetric thermal/momentum slip flow), Mukhopadhyay *et al*. [63] (on plate boundary layer mixed convection flow under transverse magnetic field with lateral mass influx), Uddin *et al.* [64] (on contracting/extending Sakiadis magneto-nanofluid biopolymer slip coating flow with Biot number effects). Bég *et al.* [65] used a collocation algorithm to compute the bioconvection nanofluid slip flow in a porous microchannel with wall deformability, considering hydrodynamic, thermal, nanoparticle and also gyrotactic micro-organism slip factors. Shukla *et al.* [66] derived homotopy solutions for Bejan entropy generation effects on hydromagnetic free and forced convective slip coating flow and heat transfer along an upright pipe. Further studies include Prakash *et al.* [67] on electro-osmotic bioinspired pumping of hybrid (multiple nanoparticles) nanofluids with internal wall slip in a microchannel and Shamshuddin *et al.* [68] on radiative magnetic polymer coating flow along an exponentially stretching sheet with power-law slip velocity and Hall current effects. Several studies have also considered rotating disk slip dynamics. Bég *et al.* [69] used an electrothermal numerical solver, PSPICE, to simulate the radiative magnetic heat transfer in Von Karman swirling slip flow with variable thermal conductivity and wall suction/blowing. Hayat *et al.* [70] used MATLAB bvp4c quadrature to analyze the swirling magneto-convective heat and mass transfer of a nanofluid from a spinning disk with velocity slip, Brownian motion and thermophoresis effects. Very

recently Recently Bég *et al.* [71] investigated numerically the Von Karman swirling bioconvective nanofluid transport from a rotating disk in a porous medium with Stefan blowing and anisotropic slip effects. The results obtained showed that the radial velocity increases whereas temperature, nanoparticle concentration and microorganism density number decrease with greater Darcy number and radial slip parameter. Micro-organism density number was however increased with the greater microorganism slip. Bég *et al.* [72] studied magneto-thermo-bioconvection of oxytactic microorganisms in nanofluid flow along a needle. Stefan blowing was applied. With elevation in Lorentzian drag force, the friction factor was reduced while the local Nusselt number, local Sherwood number, and the local motile microorganism density wall gradient were all enhanced.

Scrutiny of the existing scientific literature has revealed that, thus so far, the *Von Karman swirling slip flow of a nanofluid to a non-Darcy porous medium* has not been addressed, despite important applications in spin coating control operations. The present article therefore analyzes incompressible, steady-state rotating disk nanofluid flow, heat and mass transfer to an isotropic permeable medium with the Darcy-Forchheimer-Brinkman model. *The simultaneous inclusion of both thermal slip (jump), hydrodynamic slip, Forchheimer inertial (quadratic) drag and Brinkman vorticity diffusion effects in Von Karman swirling nanofluid flow constitutes the novelty of the present work*. The Buongiorno [73] two-component nanoscale model is implemented which features Brownian dynamics and thermophoretic body force effects. Using boundary-layer theory and appropriate transformations, robust similarity ordinary differential equations are derived which are then solved subject to physically viable boundary conditions with efficient numerical quadrature available in the bvp4c built-in function in MATLAB symbolic software. Verification of the MATLAB computations is achieved with an Adams-Moulton predictor-corrector algorithm. The impact of velocity (momentum) slip coefficient, thermal slip on all the flow controlling parameters are visualized graphically. Extensive physical interpretation of the numerical computations is provided. The current study constitutes a novel contribution to the technical literature and has to the knowledge of the authors not been communicated in the literature.

2. VON KARMAN SWIRLING NANOFLUID SLIP NON-DARCY MODEL

The steady state, incompressible slip flow, mass and energy transfer using the nanofluid induced by the rotation of an infinite perfectly flat disk is considered, as illustrated in **Fig. 1**. Rotation occurs due to the angular velocity Ω along the positive direction of φ. Edge effects are neglected. The radial direction is along r, the vertical axis is along z direction, φ is along the tangential direction, to represent the cylindrical coordinate system (r, φ, z). The infinite rough disk occupies the plane $z = 0$ and viscous incompressible nanofluid occupies the region $z > 0$ and slip conditions are adopted on the boundary. Further the boundary laeyer thickness is assumed to be is assumed to greater than the roughness at the disk. T_w indicates the wall temperature and T_∞ indicates the ambient temperature such that $T_w > T_\infty$. $t < 0$ indicates that the fluid is at rest also at constant temperature and concentration (stationary disk). The disk is then instantaneously imparted an impulsive acceleration at $t = 0$ and constant velocity. Due to this, the swirling boundary layer flow is transient during a very small interval, before reaching the well-known *steady state*. Via Buongiorno's model [73] thermophoresis and Brownian motion effects are invoked to introduce the mass deposition variation on the disk surface. Here the nanofluid is a two-component mixture comprising both a base fluid (e. g. water) and metallic nanoparticles with dilute mixture properties, negligible viscous dissipation or chemical reaction and additionally the nanoparticles and base fluid are in a sustained local thermal equilibrium. Thermophoresis and Brownian motion cannot be analyzed with other empirical nanoscale models e.g. Tiwari-Das, Maxwell-Garnetts etc. These are also essentially single-phase models since they neglect the inclusion of a species diffusion conservation equation, which is included in the Buongiorno model adopted here. Combining the models of Buongiorno [73] for nanoscale effects, Hayat *et al.* [70] for rotating disk slip flow and Umavathi and Bég [55] for non-Darcy convection flow, the governing conservation equations for the present problem become:

$$\frac{\partial u}{\partial r} + \frac{u}{r} + \frac{\partial w}{\partial r} = 0 \tag{2.1}$$

$$\rho_f \left[u\frac{\partial u}{\partial r} - \frac{v^2}{r} + w\frac{\partial u}{\partial z} \right] = -\frac{\partial P}{\partial r} + \mu_f \left[\frac{\partial^2 u}{\partial r^2} + \frac{\partial^2 u}{\partial z^2} + \frac{1}{r}\frac{\partial u}{\partial r} - \frac{u}{r^2} \right] - \frac{\mu_f}{\kappa} u - \frac{\rho_f C_f}{r\sqrt{\kappa}} u^2 \tag{2.2}$$

$$\rho_f\left[\frac{uv}{r}+u\frac{\partial v}{\partial r}+w\frac{\partial v}{\partial z}\right]=\mu_f\left[\frac{1}{r}\frac{\partial v}{\partial r}+\frac{\partial^2 v}{\partial r^2}+\frac{\partial^2 v}{\partial z^2}-\frac{v}{r^2}\right]-\frac{\mu_f}{\kappa}v-\frac{\rho_f C_f}{r\sqrt{\kappa}}v^2 \tag{2.3}$$

$$\rho_f\left[u\frac{\partial w}{\partial r}+w\frac{\partial w}{\partial z}\right]=-\frac{\partial P}{\partial z}+\mu_f\left[\frac{\partial^2 w}{\partial r^2}+\frac{\partial^2 w}{\partial z^2}+\frac{1}{r}\frac{\partial w}{\partial r}\right] \tag{2.4}$$

$$u\frac{\partial T}{\partial r}+w\frac{\partial T}{\partial z}=\alpha_f\left[\frac{\partial^2 T}{\partial z^2}+\frac{\partial^2 T}{\partial r^2}+\frac{1}{r}\frac{\partial T}{\partial r}\right]+\tau\left[\frac{D_T}{T_m}\left(\left(\frac{\partial T}{\partial r}\right)^2+\left(\frac{\partial T}{\partial z}\right)^2\right)+D_B\left(\frac{\partial C}{\partial r}\frac{\partial T}{\partial r}+\frac{\partial C}{\partial z}\frac{\partial T}{\partial z}\right)\right] \tag{2.5}$$

$$u\frac{\partial C}{\partial r}+w\frac{\partial C}{\partial z}=\frac{D_T}{T_\infty}\left[\frac{\partial^2 T}{\partial r^2}+\frac{1}{r}\frac{\partial T}{\partial r}+\frac{\partial^2 T}{\partial z^2}\right]+D_B\left[\frac{\partial^2 C}{\partial r^2}+\frac{1}{r}\frac{\partial C}{\partial r}+\frac{\partial^2 C}{\partial z^2}\right] \tag{2.6}$$

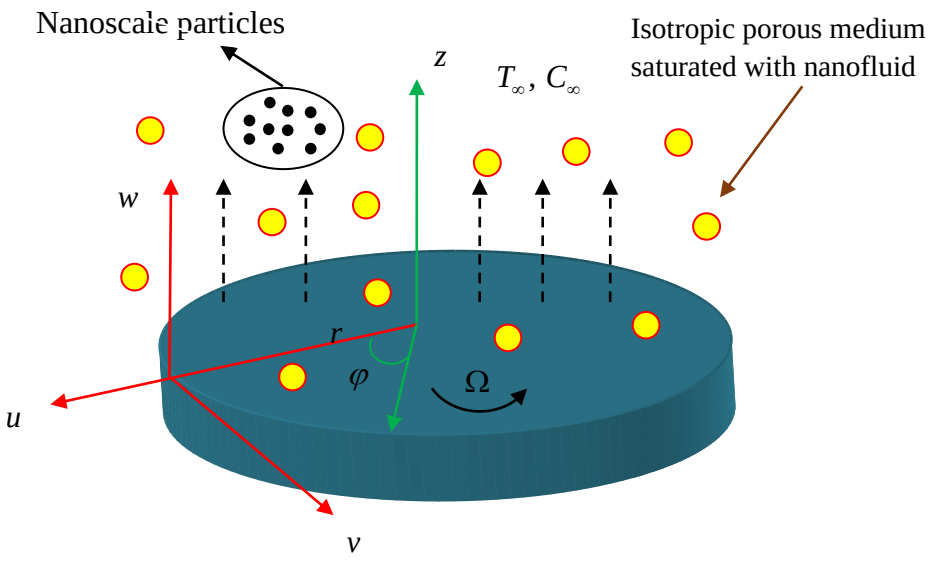

Fig.1 Physical configuration of the problem and coordinate systems

In the above equations, u denotes the velocity along radial direction, v is the velocity along tangential direction, and w represents the velocity along the vertical axis of the cylinder. The pressure is noted as p, nanoparticle concentration is taken as C, T denotes the temperature, the viscosity is taken as μ_f, the density is ρ_f, κ is the porosity, the thermal diffusivity is

represented by α_f, the ratio of heat capacity of the nanoparticle to the heat capacity of the carrying fluid is dented by τ, D_T and D_B are respectively the Brownian and thermophoretic diffusion terms α_f represents the nanofluid thermal diffusivity. The conditions on the boundary considered are

$$u = L_1 \frac{\partial u}{\partial z},\ v = L_1 \frac{\partial v}{\partial z} + r\Omega,\ \ w = 0,\ T = T_w + L_2 \frac{\partial T}{\partial z},\ D_B \frac{\partial C}{\partial z} + \frac{D_T}{T_\infty} \frac{\partial T}{\partial z} = C_h \qquad \text{at} \quad z = 0$$

$$u = 0,\ \ T \to T_\infty\ ,\ C \to C_\infty \qquad \text{at} \quad z \to \infty \tag{2.7}$$

where L_1 is the coefficient of wall slip and the coefficient of jump temperature is taken as L_2. The following similarity transformations are invoked in Eqns. (2.1) to (2.6):

$$\begin{gathered} u = r\ \Omega\, f'(\eta),\ \ v = r\ \Omega\ \ g(\eta),\ \ w = -\sqrt{2\upsilon_f \Omega}\, f(\eta),\ \eta = \sqrt{\frac{2\ \Omega}{\upsilon_f}}\ z, \\ P = P_\infty - \Omega\ \mu_f\ P(\eta),\ T = T_\infty + (T_w - T_\infty)\theta(\eta),\ \ C = C_\infty + C_\infty\, \phi(\eta) \end{gathered} \tag{2.8}$$

The dimensionless form of radial, tangential, temperature and nanoparticle concentration respectively are f, g, θ and ϕ where each one is a function of η (dimensionless axial coordinate). Equation (4) is integrated to evaluate the pressure. Equation (2.1) is already satisfied by transformations (8) while Eqns. (2.2) to (2.6) and (2.7) assume the fallowing form:

$$f''' + ff'' - \frac{1}{2}(f')^2 + \frac{1}{2} f^2 - \frac{\sigma}{2} f' - \frac{I}{2} (f')^2 = 0 \tag{2.9}$$

$$g'' + f\, g' - g\, f' - \sigma f' - I\,(f')^2 = 0 \tag{2.10}$$

$$\frac{\theta''}{\Pr} + Nb\ \theta'\phi' + Nt(\theta')^2 + \ f\,\theta' = 0 \tag{2.11}$$

$$\phi'' + Sc\ \ f\phi' + \frac{Nt}{Nb}\theta'' = 0 \tag{2.12}$$

The emerging boundary conditions assume the form:

$$\begin{gathered} f(\eta) = 0,\ f'(\eta) = \gamma\ \ f''(\eta),\ g(\eta) = 1 + \gamma\, g'(\eta),\ \theta(\eta) = 1 + \alpha\, \theta'(\eta), \\ \phi'(\eta) + \frac{Nt}{Nb}\theta'(\eta)\ = 0 \end{gathered} \qquad \text{at} \quad \eta = 0 \tag{2.13}$$

$$f'(\infty) = 0,\ g(\infty) = 0,\ \theta(\infty) = 0,\ \ \phi(\infty)\ = 0,\ \ P(\infty)\ = 0 \qquad \text{at} \quad \eta = \infty \tag{2.14}$$

In this prime indicates derivative with respect to η, the inertial drag parameter is I, σ is the Darcian (inverse permeability) number, the thermophoresis and Brownian parameters are Nt and Nb, Sc denotes the Schmidt number, Re represents the rotational Reynolds number, The slip velocity and slip temperature are denoted as γ and α, the Prandtl parameter is Pr and are defined as follows.

$$I = \frac{C_f}{\sqrt{\kappa}}, \sigma = \frac{\upsilon_f}{\Omega \kappa}, \ Re = \frac{\Omega r^2}{\upsilon_f}, Nb = \frac{(\rho C)_p \ D_B (C_w - C_h)}{(\rho C)_f \ \upsilon}, Nt = \frac{(\rho C)_p \ D_T \ (T_w - T_h)}{(\rho C)_f \ T_m \upsilon},$$
$$Sc = \frac{\upsilon_f}{D_B}, Pr = \frac{\upsilon_f}{\alpha_f}, Y = L_1 \sqrt{\frac{2\Omega}{\upsilon_f}}, \alpha = L_2 \sqrt{\frac{2\Omega}{\upsilon_f}} \tag{2.15}$$

Important physical parameters are skin friction coefficient C_{fr} and reduced Nusselt number Nu_r for coating dynamics and these are defined as below:

$$C_{fr} = \frac{\sqrt{\tau_r^2 + \tau_0^2}}{\rho_f (r\Omega)^2}, \ Nu_r = \frac{r \, q^{"}}{k(T_w - T_\infty)} \tag{2.16}$$

Here τ_r is radial stress, τ_∞ is tangential stress and $q^{"}$ represents the heat flux from the disk, (based on the Fourier law) which take the following definitions:

$$\tau_r = \mu_f \left(\frac{\partial u}{\partial z} + \frac{\partial w}{\partial r} \right)\Bigg|_{z=0}, \ \tau_\theta = \mu_f \left(\frac{\partial v}{\partial z} + \frac{\partial w}{\partial r} \right)\Bigg|_{z=0}$$
$$q'' = -k \left(\frac{\partial T}{\partial z} \right)\Bigg|_{z=0} \tag{2.17}$$

For the present problem, the emerging expressions for skin friction coefficient and Local Nusselt number in terms of the variables defined in Eqn. (2.6) become:

$$C_{fr} = \frac{1}{\sqrt{\left(\frac{2 \ \Omega \ r^2}{\upsilon_f} \right)}} \sqrt{\left(g'(0)^2 + f''(0)^2 \right)}, \qquad Nu_r = -r \sqrt{\frac{2\Omega}{\upsilon_f}} \ \theta'(0) \tag{2.18}$$

Of course, a separate expression for nanoparticle mass transfer rate may be derived i. e. for Sherwood number, However, for brevity, here we restrict attention to the primitive variable i. e. nanoparticle concentration, $\phi(\eta)$.

3. NUMERICAL SOLUTION WITH MATLAB BVP4C SOLVER

The three-stage Lobatto IIIA formula is adopted in BVP$C solver in MATLAB. The error control and the size of the mesh are dependent on the residue of the continuous solution. The continuous solution is obtained from the collocation polynomial which uses the fourth order accuracy in the interval [a, b]. The procedure followed is that the nonlinear differential equations are rewritten in the form of first-order differential equations introducing the new variables. The error tolerance is to the order of eight decimal places. After the compilation of the code, the solution is placed in the buffer called sol. y and the buffer sol. x contains the information of the mesh selection. Uddin *et al*. [74] is used to verify and confirm that the residual is less than the tolerance or not. The value of Y_{MID} and the gradient at the ends of the subinterval is computed by Bvp5c. Russell and Christansen [75] used the following stepping formula to calculate Y_{MID}.

$$Y_{MID} = Y_1 + \zeta\left[\frac{17}{192}K_1 + \frac{40+15\sqrt{5}}{192}K_2 + \frac{40+15\sqrt{5}}{192}K_3 - \frac{1}{192}K_4\right] \tag{3.1}$$

Here Y_1 is the initial guess and K_1, K_2, K_3, K_4 are the approximations with a stepping distance of ζ. Excellent stable solutions are generated for radial, azimuthal and axial velocity, temperature and nanoparticle concentration in **Figs. 2-18**. Further details of the MATLAB bvp4c shooting algorithm are reviewed with many applications in multi-physical fluid dynamics by Bég [76], and Sarkar and Sahoo [77].

4. VALIDATION WITH ADAMS–MOULTON 2-STEP PRED-CORR SCHEME

Since the present model is novel, there are no solutions against which to benchmark the BVP4C finite difference results. To validate the computations, therefore, an alternate numerical method is deployed, namely the Adams Moulton predictor-corrector method, which is described in Pal [78]. This verification approach also has the significant advantage that the full model developed in the current work can be validated i. e. with *non-Darcy and nanofluid effects*, rather than a very

restricted model from the literature which does not features all the multi-physics. The Adams Moulton method is an implicit multistep method. A popular version is the rapidly convergent, stable 2-step Adams Moulton method for a linear initial value problem. Applying this algorithm to the present boundary value problem, we define the gradients of the *dimensionless f, g, θ and ϕ* as follows using a general function, *v*:

$$\frac{df}{d\eta} = \nu(\eta, f), \; f(\eta_0) = f_0 \tag{4.1}$$

$$\frac{dg}{d\eta} = \nu(\eta, \theta), \; g(\eta_0) = g_0 \tag{4.2}$$

$$\frac{d\theta}{d\eta} = \nu(\eta, \theta), \; \theta(\eta_0) = \theta_0 \tag{4.3}$$

$$\frac{d\phi}{d\eta} = \nu(\eta, \phi), \; \phi(\eta_0) = \phi_0 \tag{4.4}$$

Here $f_0, g_0, \theta_0, \phi_0$ are initial guesses. The *predictors* are then specified and thereafter the correctors to produce an accurate solution based on the initial calculation. The Adams-Moulton two-step *predictor relations* for the four variables, with a stepping distance of ζ, take the form:

$$f_{k+1} = f_k + \frac{\zeta}{2}\left(3\nu(\eta_k, f_k) - \nu(\eta_{k-1}, f_{k-1})\right) \tag{4.5}$$

$$g_{k+1} = g_k + \frac{\zeta}{2}\left(3\nu(\eta_k, g_k) - \nu(\eta_{k-1}, g_{k-1})\right) \tag{4.6}$$

$$\theta_{k+1} = \theta_k + \frac{\zeta}{2}\left(3\nu(\eta_k, \theta_k) - \nu(\eta_{k-1}, \theta_{k-1})\right) \tag{4.7}$$

$$\phi_{k+1} = \phi_k + \frac{\zeta}{2}\left(3\nu(\eta_k, \phi_k) - \nu(\eta_{k-1}, \phi_{k-1})\right) \tag{4.8}$$

The corresponding two-step *corrector* formulae are given by:

$$f_{k+1} = f_k + \frac{\zeta}{2}\left(\nu(\eta_{k+1}, f_{k+1}) - \nu(\eta_k, f_k)\right) \tag{4.9}$$

$$g_{k+1} = g_k + \frac{\zeta}{2}\left(\nu(\eta_{k+1}, g_{k+1}) - \nu(\eta_k, g_k)\right) \tag{4.10}$$

$$\theta_{k+1} = \theta_k + \frac{\zeta}{2}\left(\nu(\eta_{k+1}, \theta_{k+1}) - \nu(\eta_k, \theta_k)\right) \tag{4.11}$$

$$\phi_{k+1} = \phi_k + \frac{\zeta}{2}\left(\nu\left(\eta_{k+1},\phi_{k+1}\right) - \nu\left(\eta_k,\phi_k\right)\right) \tag{4.12}$$

The trapezoidal rule is also used to refer the AM2 (Adams-Moulton of second order accuracy) which is an implicit scheme. For a non-linear boundary value problem, *non-linear algebraic equations* are solved at each step iteratively. To verify the MATLAB bvp4c solutions, the results in **Tables 1-2** are compared with the Adams Moulton predictor corrector method (AMPC). A tolerance of 10^{-8} is also set in the AMPC code running on a 4 quad processor Acer laptop. Computations converge in seconds.

TABLE 1a and 1b Comparison BVPC and AMPC for various σ, I, γ, Pr for $Nt = 0.2, \sigma = I = 4, Nb = 0.5, Sc = 10, \alpha = 0.25$, *Pr = 7 (aqueous nanofluid).*

TABLE 1a.

σ	I	γ	$f''(0)$ BVP4C	$f''(0)$ AMPC	$f'(0)$ BVP4C	$f''(0)$ AMPC	$g'(0)$ BVP4C	$g'(0)$ AMPC
0.0	4.0	0.25	0.2085192	0.2085192	0.0521298	0.0521297	-0.4445535	-0.4445531
2.0	4.0	0.25	0.13347139	0.13347143	0.03336785	0.03336783	-0.4890830	-0.4890831
4.0	4.0	0.25	0.1037314	0.1037314	0.0259328	0.0259328	-0.5120709	-0.5120708
6.0	4.0	0.25	0.0867979	0.0867979	0.0216994	0.0216994	-0.5268938	-0.5268938
4.0	0.0	0.25	0.1056118	0.1056118	0.0264029	0.0264029	-0.5103965	-0.5103965
4.0	2.0	0.25	0.1046495	0.1046495	0.0261623	0.0261623	-0.5112519	-0.5112519
4.0	4.0	0.25	0.1037314	0.1037314	0.0259328	0.0259327	-0.5120709	-0.5120709
4.0	6.0	0.25	0.1028536	0.1028536	0.0257134	0.0257133	-0.5128567	-0.5128567
4.0	4.0	0	0.1877161	0.1877161	0.0000000	0.0000000	-0.5496780	-0.5496780
4.0	4.0	0.2	0.1155049	0.1155049	0.0231009	0.0231001	-0.5229057	-0.5229057
4.0	4.0	0.4	0.0772842	0.0772842	0.0309137	0.0309137	-0.4778066	-0.4778066
4.0	4.0	0.6	0.0551019	0.0551018	0.0330611	0.0330612	-0.4341933	-0.4341933

TABLE 1b.

σ	I	α	Pr	Nt	$\theta'(0)$ BVP4C	$\theta(0)$ AMPC
0.0	4.0	0.25	7	0.2	-0.51861923	-0.51861930
2.0	4.0	0.25	7	0.2	-0.37580753	-0.37580755
4.0	4.0	0.25	7	0.2	-0.29661539	-0.29661544
6.0	4.0	0.25	7	0.2	-0.24690272	-0.24690268
4.0	0.0	0.25	7	0.2	-0.30122598	-0.30122596
4.0	2.0	0.25	7	0.2	-0.29886922	-0.29886924
4.0	4.0	0.25	7	0.2	-0.29661539	-0.29661535
4.0	6.0	0.25	7	0.2	-0.29445602	-0.29445605
4.0	4.0	0	7	0.2	-0.31506696	-0.31506689
4.0	4.0	0.2	7	0.2	-0.30018501	-0.30018499
4.0	4.0	0.4	7	0.2	-0.28626302	-0.286262897
4.0	4.0	0.6	7	0.2	-0.27327074	-0.27327071
4.0	4.0	0.25	10	0.2	-0.35684831	-0.35684838
4.0	4.0	0.25	8	0.2	-0.31818077	-0.31818071
4.0	4.0	0.25	6	0.2	-0.27326416	-0.27326414
4.0	4.0	0.25	5	0.2	-0.24791602	-0.24791606
4.0	4.0	0.25	7	0.1	-0.32588972	-0.32588973
4.0	4.0	0.25	7	0.3	-0.26817915	-0.26817912
4.0	4.0	0.25	7	0.5	-0.21648707	-0.21648704
4.0	4.0	0.25	7	0.7	-0.17461625	-0.17461621

Excellent correlation is achieved for each Table testifying to the accuracy of the BVP4C MATLAB solver technique which is adopted for all graphical visualizations in the next section. In Table 1a, 1b we tabulated the values of unknown function $f'(0)$, $f''(0)$ and $g'(0)$ for different parameters. Increasing the values of inverse permeability and inertial parameter, *radial, axial and tangential shear stress coefficients* are decreased since decreasing permeability

(higher σ) and greater Forchheimer drag (I) decelerate the flow on the disk surface. The radial stress, represented by $f''(0)$ decreases, $f'(0)$ increases and also $g'(0)$ increases with increasing velocity slip coefficient, γ. In Table 1b, it is observed that elevation in σ (i. e reduction in permeability), i I , α , Pr and Nt , decrease the reduced Nusselt number. It is noteworthy that smaller permeability intensifies the quantity of solid fibers in the porous medium which enhances temperatures in the boundary layer- this leads to a depletion in heat transferred to the disk surface i. e. lower Nusselt numbers.

5. RESULTS AND DISCUSSION

The impact of the key thermophysical and hydrodynamic parameters γ , σ , I , α , Nb , Nt , Sc and Pr on the *radial, tangential, axial velocity, temperature and nanoparticle concentration field distributions* as computed with BVP4C MATLAB quadrature are visualized in **Figures 2-18.** The values chosen are $A = 0.25, \sigma = 4.0, Nt = 0.2, Nb = 0.5, Sc = 1.0, I - 4.0, \gamma = 0.25$ except the varying parameter in all the pictures.

Figure 2 shows the variation in radial velocity for different values of velocity (momentum) slip parameter γ . Owing to the presence of wall slip effects, the radial velocity exists at the disk although there is no stretching along the radial direction. As γ is magnified, velocity declines and the paramount velocity moves towards the disk surface. The effect of velocity slips parameter γ on the tangential velocity is shown in Fig 3; significant depletion is computed when slip parameter γ is increased. Therefore, both radial and tangential (azimuthal) deceleration is induced in the boundary layer flow along the disk. This indicates that in the absence of slip effects, *over-prediction in velocity components* is produced which furnishes unrealistic information for designers.

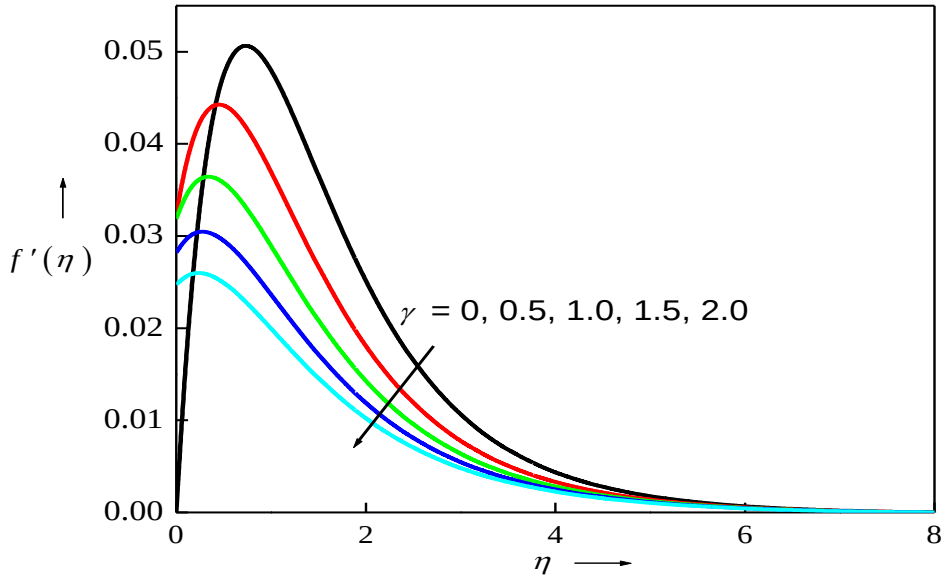

FIGURE 2 Chart of radial velcoity for distinct γ

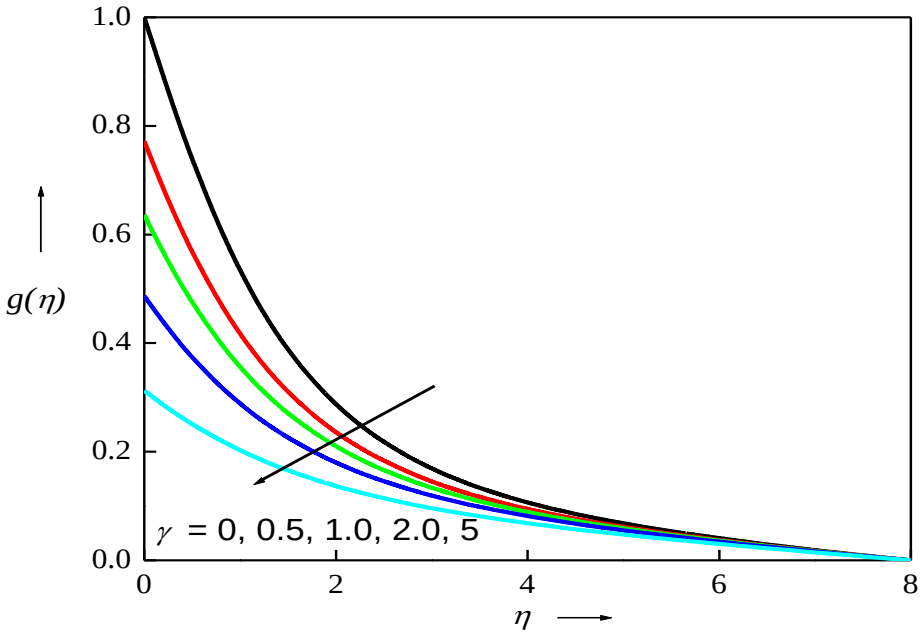

FIGURE 3 Chart of tangential velcoity for distinct γ.

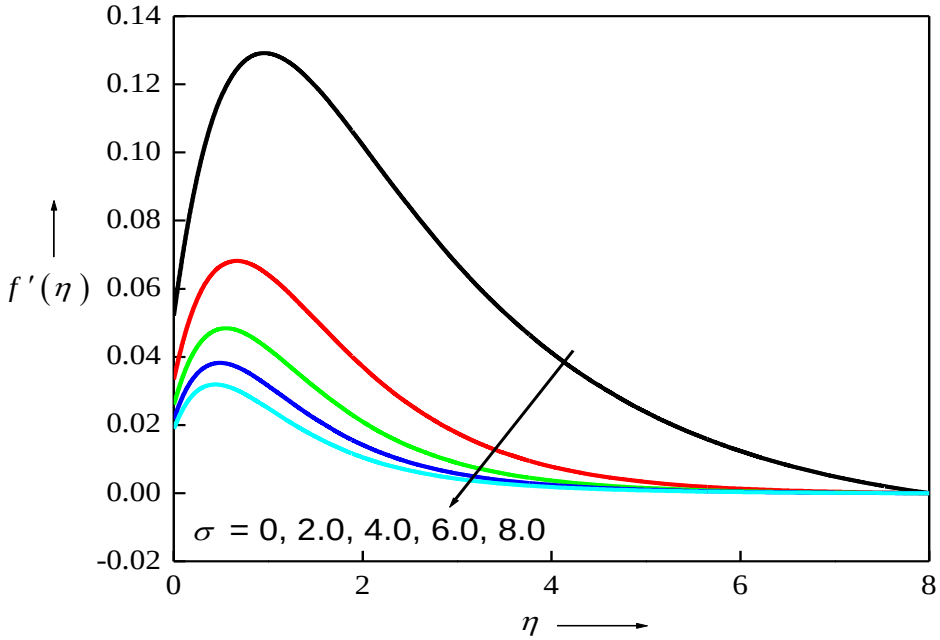

FIGURE 4 Chart of radial velocity for distinct σ.

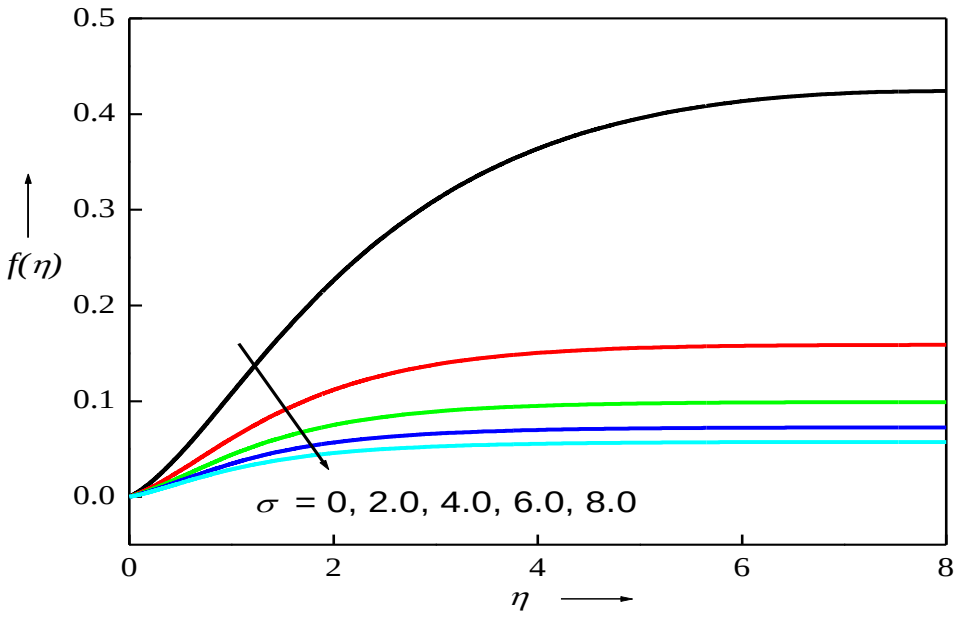

FIGURE 5 Chart of axial velocity for distinct σ.

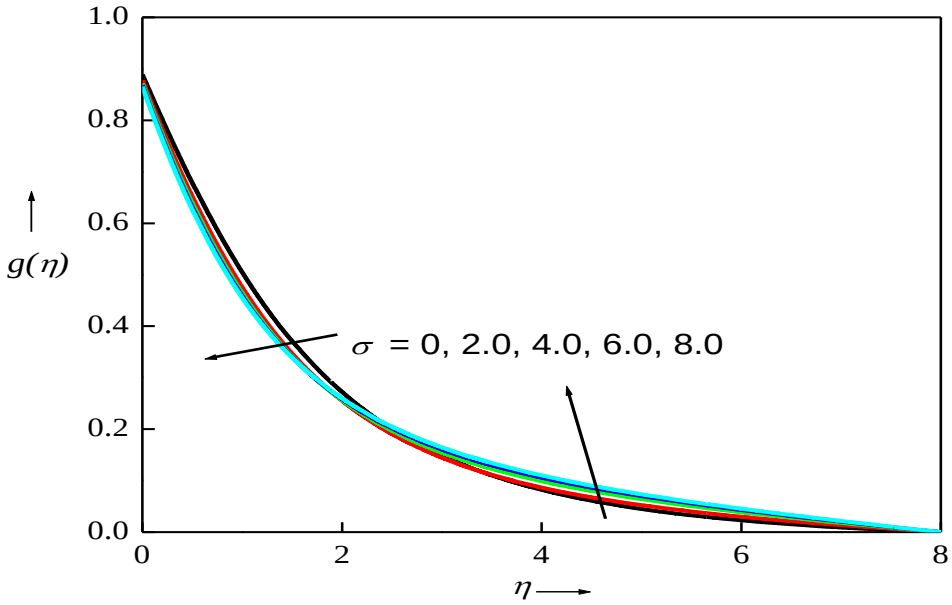

FIGURE 6 Chart of tagentail velocity for distinct σ.

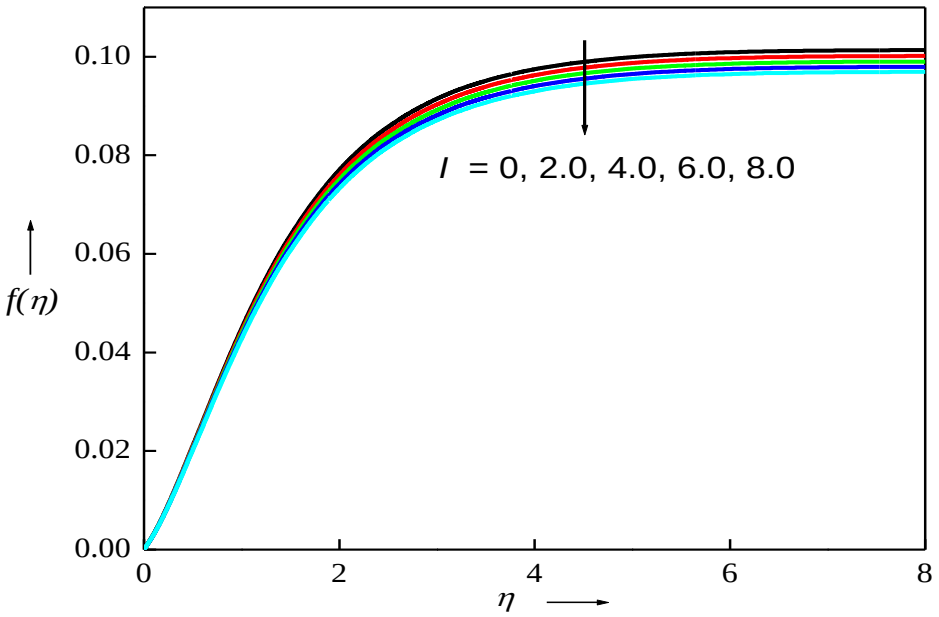

FIGURE 7 Chart of tagentail velocity for distinct I.

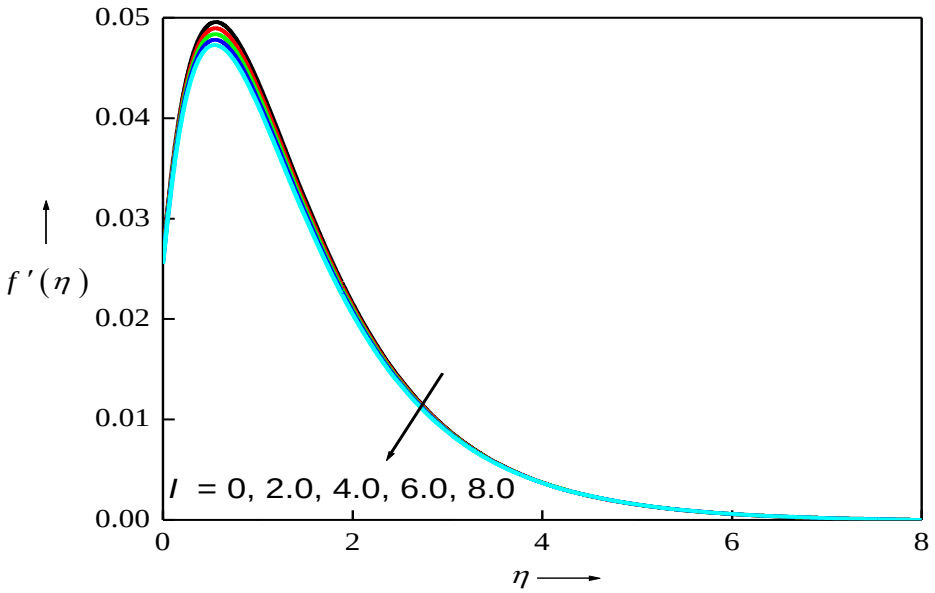

FIGURE 8 Chart of radial velocity for distinct *I*.

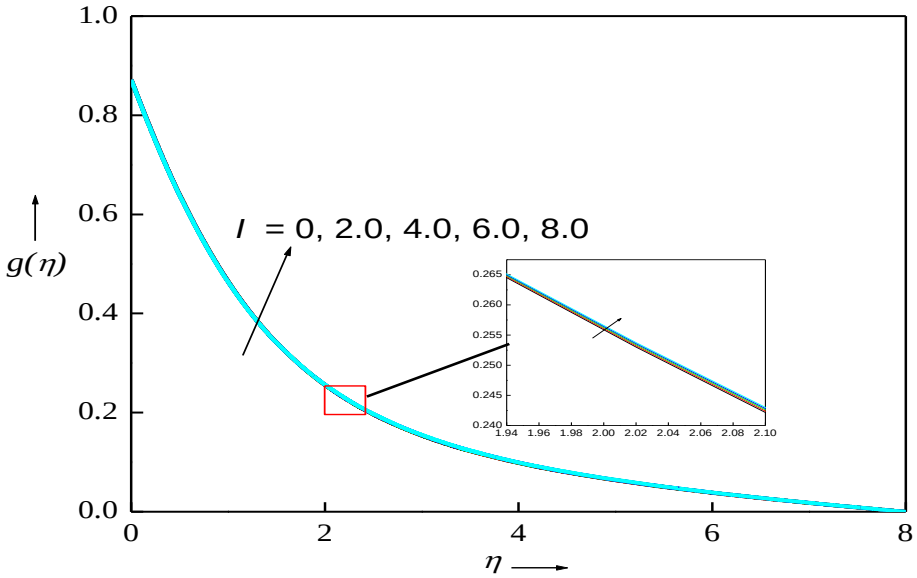

FIGURE 9 Chart of tagentail velocity for distinct *I*.

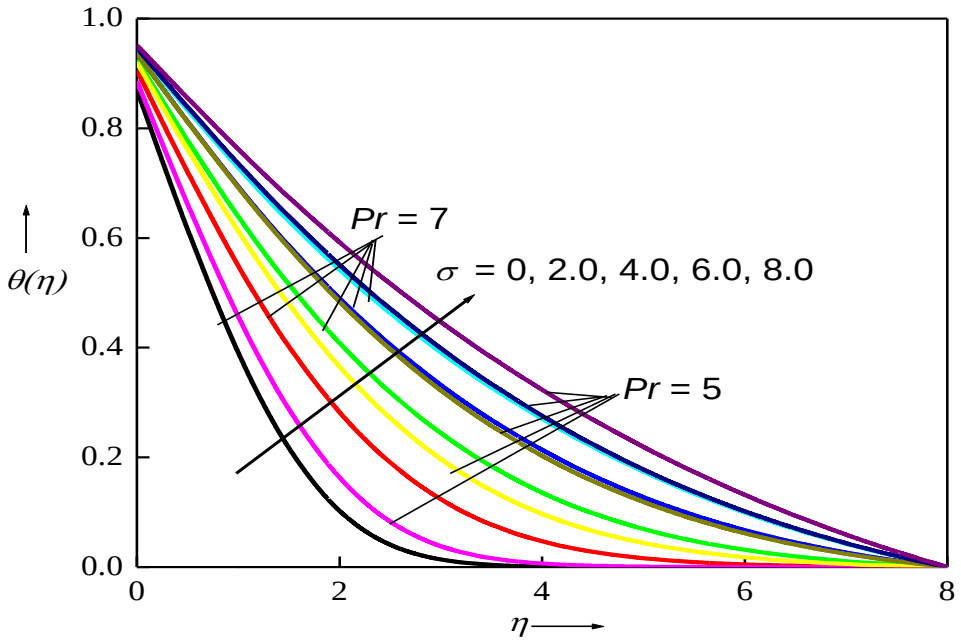

FIGURE 10 Chart of temperature for disntict σ.

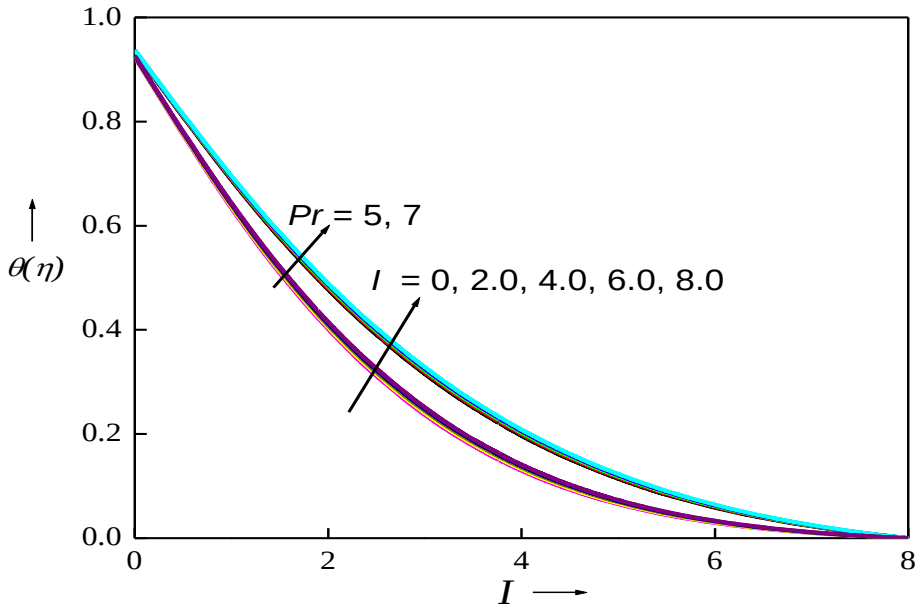

FIGURE 11 Chart of temperature for different distinct *I*.

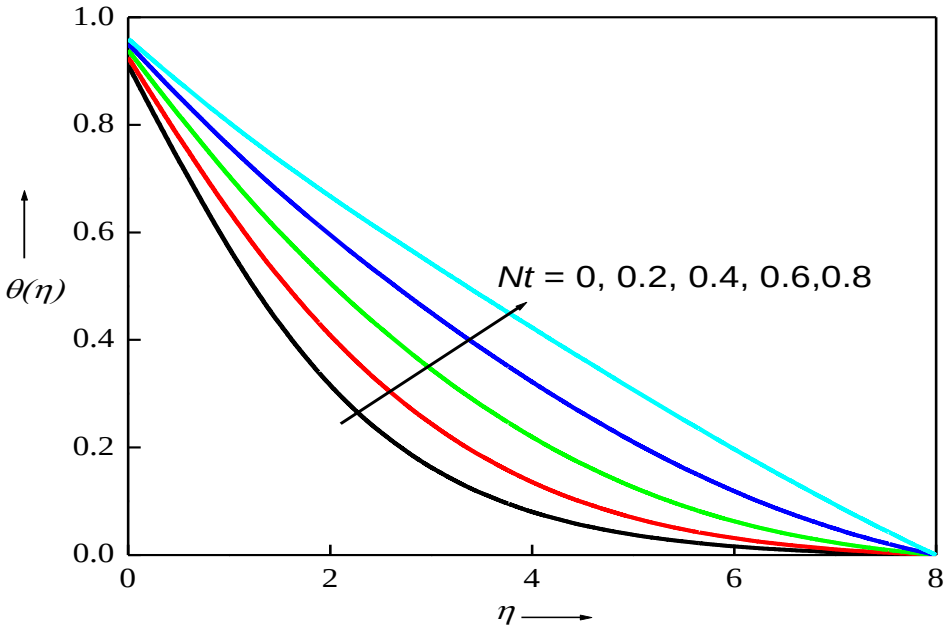

FIGURE 12 Chart of temperature for distinct *Nt*.

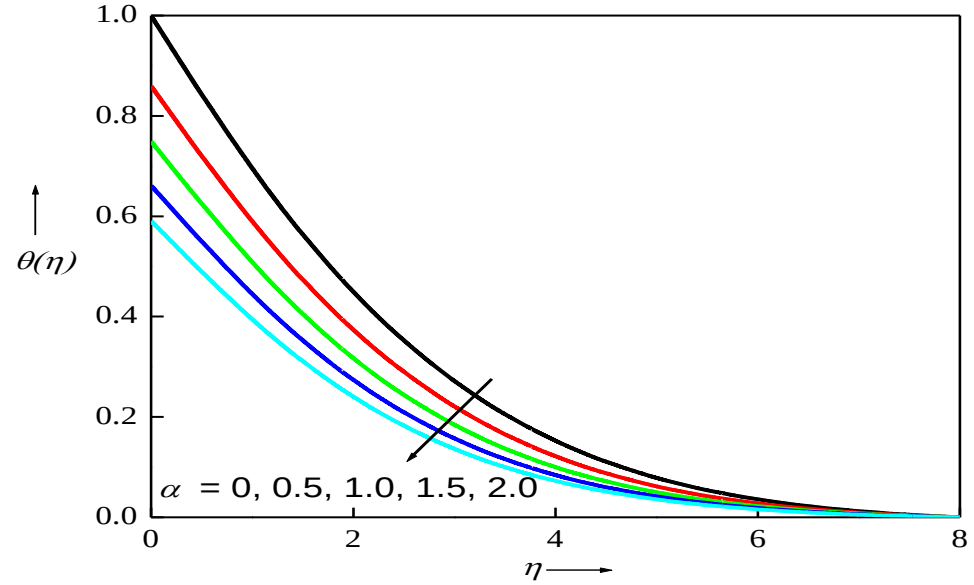

FIGURE 13 Chart of temperature for distinct α.

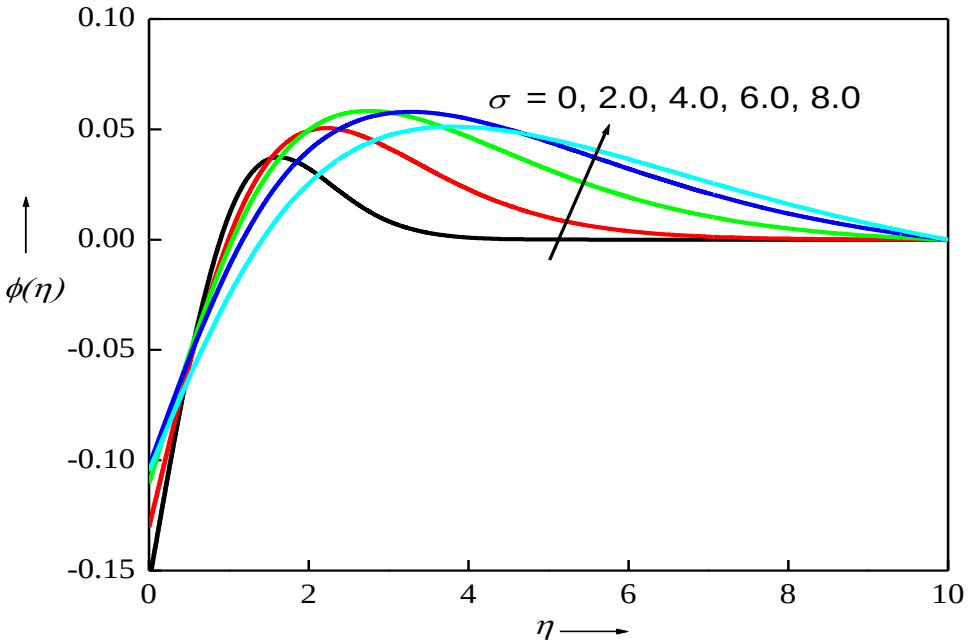

FIGURE 14 Chart of concentration for distinct σ.

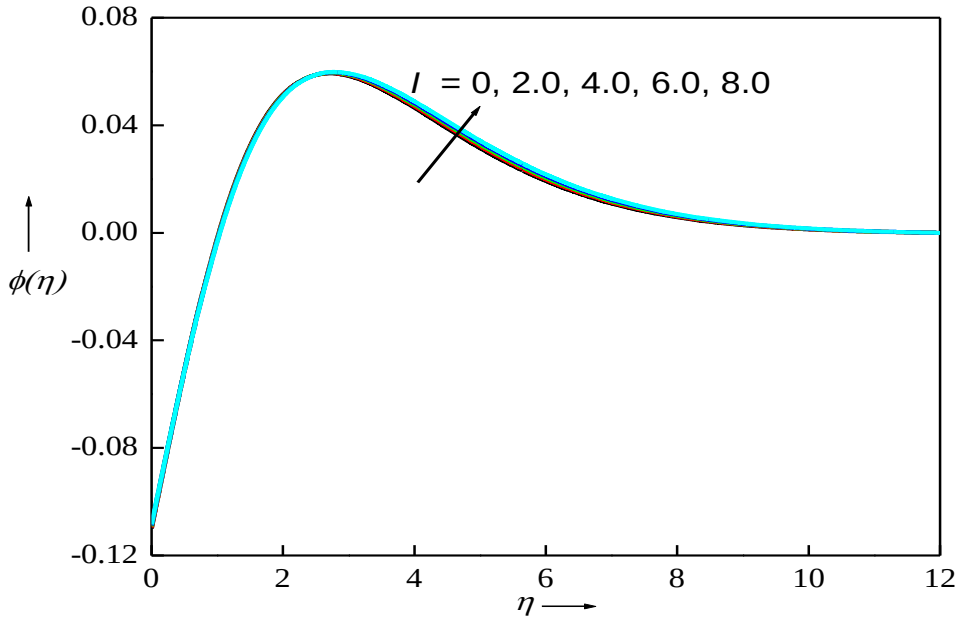

FIGURE 15 Chart of concentration for distinct I.

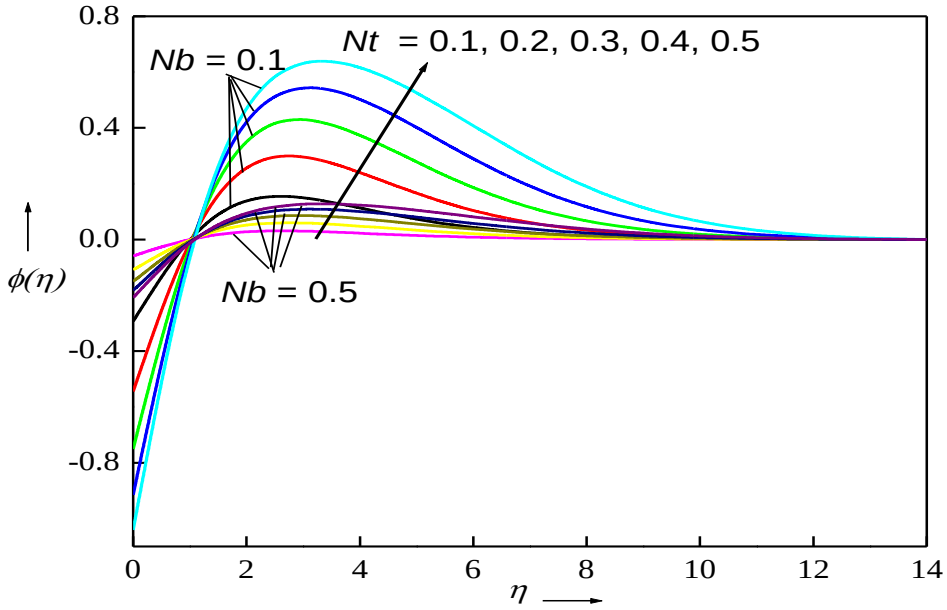

FIGURE 16 Chart of concentration for distinct *Nt*.

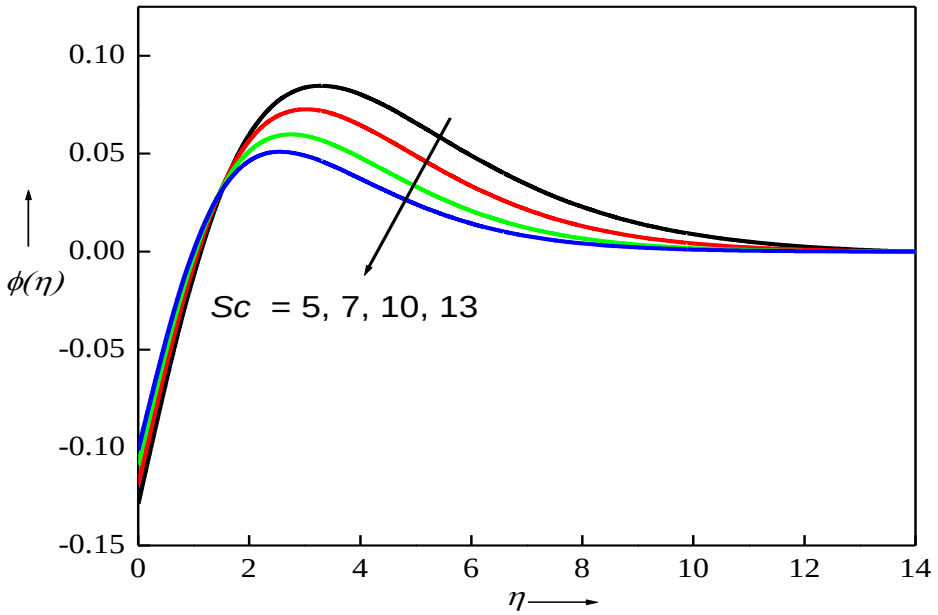

FIGURE 17 Chart of concentration for distinct *Sc*.

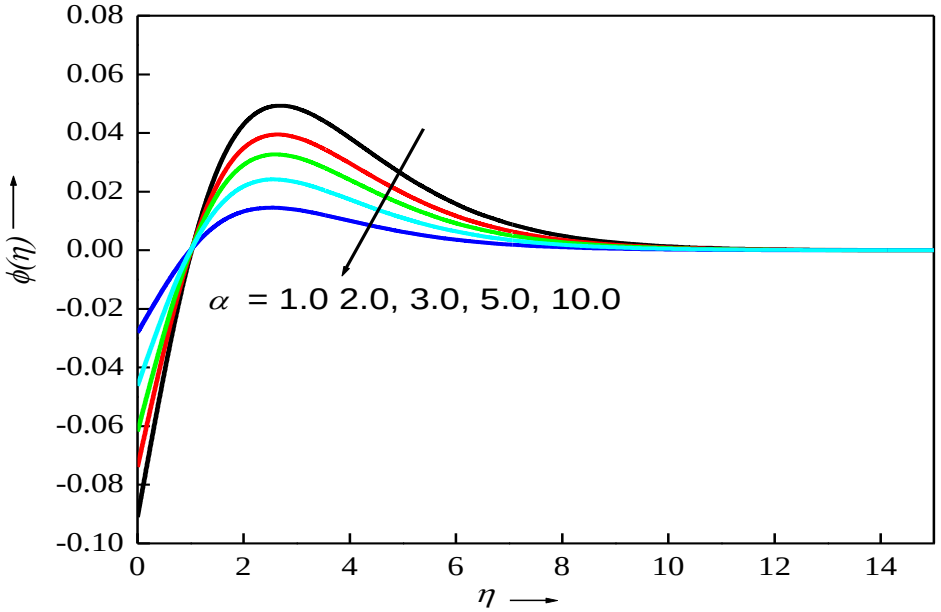

FIGURE 18 Chart of concentration for distinct α.

In **Fig. 4-6**, impacts of inverse permeability parameter σ on the radial velocity, axial velocity and tangential velocity profiles are shown. The influence of inverse permeability parameter σ is similar but more pronounced than that of velocity slip parameter γ i. e. they are qualitatively similar. A consistent decrement in both radial and axial velocity is induced (Figs. 4, 5) at all values of transverse coordinate. The enhancement in *inverse Darcy parameter* implies a reduction in medium permeability. This produces larger bulk drag resistance to the flow. However, while initially the tangential velocity Fig. 6) is initially stifled, again with higher Darcian impedance forces associated with higher σ values; however further from the disk the reverse behavior is induced. The rotating disk system acts similar to a *fan configuration drawing fluid axially inward from the surrounding medium towards the disk surface*. Since no transpiration occurs at the disk surface i. e. *it is solid*, therefore the incoming nanofluid is turned and *discharges in the radial direction* along the disk. This results in a re-distribution in momentum which produces radial flow acceleration further from the disk surface and counteracts the bulk porous medium drag.

In **Figs 7-9**, the variation in inertial parameter I on the axial velocity, radial velocity and tangential velocity are depicted. As increasing the values of inertial parameter I axial velocity

decreases and this trend is amplified further from the rotating disk surface as shown in Fig 7. For large values of I , the radial velocity condenses and also the ultimate velocity will bend near the rotating wall. However, there are less pronounced modifications in the tangential velocity as compared with the axial and radial velocity as shown in Fig 9. While the Darcian parameter, σ appears in the linear drag force term and simulates the linear drag effect of the bulk porous media fiber resistance at low Reynolds number on the nanofluid, the Forchheimer parameter is quadratic and exerts a more substantial retarding effect. Of course, in the limit when $\kappa \to \infty$ (and of course when Forchheimer quadratic drag parameter, $I \to 0$) the solid fibers vanish and the regime is purely nanofluid. Although the Forchheimer second order drag term which appears in the momentum boundary layer Eqn. increases with inertial effect i.e. greater Reynolds number, it is not associated with acceleration of the flow. The overwhelming influence of I is to decelerate the swirling flow in the porous regime. This is characteristic of Forchheimer effects.

It is also pertinent to note that the range of I values considered does not stimulate *vortex formation* associated with higher Reynolds numbers (greater than 250). However, the boundary layers around the pores become more pronounced and an "inertial core" appears with higher Forchheimer number. The developing of these "core" flows external to the boundary layers accounts for the *non-linear relationship* between pressure drop and flow rate. Strong regulation of the coating velocity field therefore is achievable by pressure generated inertial effects in the porous medium.

The variation in the temperature filed with the increase in inverse permeability parameter σ is visualized in **Fig. 10**. In contrast with the velocity field, the heat magnitudes are increased by boosting σ since the smaller permeability's imply greater concentration of solid matrix fibers. This encourages thermal conduction which manifests in heating of the nanofluid and elevation in temperatures. Increment in Prandtl number also elevates temperatures.

Figure 11 display the characteristic of I on the energy distribution. Increasing the values of inertial parameter I strongly elevate temperatures. Again, this is due to the deceleration in the flow associated with stronger Forchheimer drag. The decrease in momentum diffusion rate allows better convective heat transfer in the medium and energizes the flow. Temperatures are therefore enhanced consistently at all values of transverse coordinate.

The issue of Nt (defines the ratio of thermophoretic diffusion to the momentum diffusion) on the energy field is presented in **Fig. 12**. The nanoparticles immigrate from hot zone to the cold zone when exposed to the temperature gradient. The temperature magnitudes are boosted and there is a corresponding increase in thermal boundary layer thickness as the values of Nt are augumented. **Figure 13** depicts the effect of thermal slip parameter α on thermal boundary layer. The heat transfer is receded from the disk to the neighboring fluid layers by expanding α. Since the thermal penetration distance is increased with thermal jump, and this leads to a reduction in temperature magnitudes. Thermal boundary layer thickness is therefore also depleted with greater thermal jump (slip) effect.

Figure 14 shows the response in nanoparticle concentration to variation in inverse permeability parameter σ. The impact of σ makes the nanoparticle concentration to attain negative values which physically infer that the ambient concentration C_∞ is larger than the wall concentration. The nanoparticle concentration increases, and the location of the absolute maximum is displaced at a distance from the boundary as the inverse permeability parameter σ is increased. **Figure 15** illustrates the influence of Forchheimer inertial parameter I on the nanoparticle concentration field. As increasing the values of inertial parameter I the concentration magnitudes also increase. Species diffusion of nanoparticles is therefore encouraged with flow deceleration and results in greater nanoparticle boundary layer thickness.

For incremental values of Nt results in the expansion of the nanoparticle concentration as figured in **Fig. 16**. Further the utmost values of the contours are tending far away form the disk surface. This figure also inform that the nanoparticle concentration field is declined for enlarging the Brownian motion parameter Nb. Higher values of Nb imply smaller nanoparticle dimensions in the Buongiorno model. Nanoparticle species boundary layer thickness is decreased with greater Brownian motion effect. **Figure 17** visualizes the profiles of nanoparticle concentration for various values of Sc (Sc is the inverse of D_B). The concentration boundary layer thickness is dwindled by raising the Schmidt number. Whereas near the disk surface a slight enhancement in nanoparticle concentration is induced, the dominant effect for the majority of the boundary layer regime is the decrease in nanoparticle concentration magnitudes with greater Schmidt number. **Figure 18**. presents the distribution in nanoparticle concentration for various values of thermal slip parameter α. As the thermal jump effect is intensified i. e. α

enlarges, nanoparticle concentration field shrinks substantially and the contours attaining the optimum values tend to depart away from the wall. Nanoparticle boundary layer thickness is therefore also reduced with stronger thermal slip effect. The implication is that when mathematical models neglect thermal slip, an over-estimate is produced in computations. This is avoided by inclusion of a correct thermal slip feature in the disk surface boundary conditions as reported here.

6. CONCLUSIONS

A theoretical and computational study of the steady heat and mass transfer in Von Karman swirling slip flow of a nanofluid from a rotating disk adjacent to a homogenous non-Darcy porous medium has been presented. The porous medium is simulated with a Darcy-Forchheimer-Brinkman model. Thermophoresis and Brownian dynamics of the nanoparticles have been simulated with the Buongiorno nanoscale model. Von Karman similarity variables are deployed to transform the partial differential conservation equations into a system of highly coupled, nonlinear, dimensionless ordinary differential equations (ODE's). These similarity boundary layer equations i. e. continuity, momentum, energy and nanoparticle concentration (volume fraction) are solved with bvp4c shooting quadrature in MATLAB. Validation with earlier studies is included. Further verification with an Adams-Moulton predictor-corrector method is conducted. The influence of *velocity (momentum) slip coefficient, thermal slip, Darcian bulk drag parameter (inverse permeability), Forchheimer inertial parameter, thermophoresis and Brownian motion parameters, Schmidt number, Prandtl number,* on *radial, tangential (azimuthal) and axial velocity components, temperature and nanoparticle concentration* are visualized graphically. The distributions for skin friction components, Nusselt number (dimensionless heat transfer rate at the disk surface) are also computed. The present computations have shown that:

1)Radial, axial and tangential velocities are reduced with increasing Forchheimer inertial drag and hydrodynamic wall slip whereas they are elevated with increasing permeability (decreasing inverse Darcy parameter).

2) Thermal and nanoparticle concentration boundary layers are also markedly modified with increasing Forchheimer inertial parameter, Prandtl number, Schmidt number, Brownian motion parameter and thermophoresis parameter.
3) Nanoparticle boundary layer thickness is therefore also reduced with stronger thermal slip effect.
4) Species diffusion of nanoparticles is therefore encouraged with flow deceleration and results in greater nanoparticle boundary layer thickness.
5) With increasing inverse permeability parameter (i. e. smaller permeabilities and greater concentration of solid matrix fibers), thermal conduction is boosted and this results in elevation in nanofluid temperatures.
6) An increment in Forchheimer inertial parameter also strongly elevate temperatures and this is attributable to the strong flow deceleration with stronger Forchheimer drag. The decrease in momentum diffusion rate allows better convective heat transfer in the medium and energizes the flow leading to greater thermal boundary layer thickness.
7) Although radial velocity and axial velocity are suppressed quite strongly with increasing inertial inertial parameter, there is a less pronounced modifications in the tangential velocity.

The present study has revealed some interesting characteristics of Von Karman swirling flow in nanofluid-saturated porous media adjacent to a rotating disk of relevance to nanomaterial spin coating. However, the analysis has been confined to *steady state flow* and has *neglected surface tension and chemical reaction effects* (Jensen *et al.* [79]). In practical spin coating operations, the viscosity of the nanofluid and surface tension results in evaluating the thickness of the film. The baking at high temperatures and spinning process causes the removal of the solvent. These non-Newtonian nanofluid aspects (Guha and Sengupta [80]) may be investigated in future studies for which **MATLAB BVP4C** quadrature is also a promising numerical approach.

CONFLICT OF INTEREST

This work does not have any conflict of interest

REFERENCES

1. Von Karman T. Uber laminare and burbulente Reibung (On laminar and turbulent flow). Z. Angew. Math. Mech. 1921;1:233-252.
2. Wagner C. Heat transfer from a rotating disk to ambient air. J Appl Phys. 1948;19: 837–839.
3. Cobb EC, Saunders OA. Heat transfer from a rotating disk. Proc. Royal Society. 1956; 236:343-351.
4. Millsaps K, Pohlhausen K. Heat transfer by laminar flow from a rotating plate. J. Aeronautical Science. 1952;19:120-126.
5. Kobayashi R, Kohama Y, Takamadate Ch. Spiral vortices in boundary layer transition regime on a rotating disk. Acta Mech. 1980; 35:71-82.
6. Awad MM. Heat transfer from a rotating disk to fluids for a wide range of Prandtl numbers using the asymptotic model. ASME J. Heat Transfer. 2008;130: 014505.
7. Greif R, Paterson J. Mass transfer to a rotating disk in a non-Newtonian fluid. Phys. Fluids. 1973;16:1816-1817.
8. Mishra P, Singh P. Mass transfer from rotating disk to non-Newtonian fluids. Chem. Eng. Sci. 1978;33:1463-1470.
9. He Y, Ma L, Huang S. Convection heat and mass transfer from a disk. Heat and Mass Transfer. 2005;41:766–772.
10. Rashaida AA, Bergstrom DJ, Sumner RJ. Mass transfer from a rotating disk to a Bingham fluid. ASME J. Appl. Mech. 2006;73:108-111.
11. Turkyilmazoglu M. MHD fluid flow and heat transfer due to a stretching rotating disk. Int. J. Thermal Sci. 2012;51:195-201.
12. Bég OA, Zueco J, López-Ochoa LM. Network numerical analysis of optically thick hydromagnetic slip flow from a porous spinning disk with radiation flux, variable thermophysical properties and surface injection effects. Chemical Engineering Communications. 2011;3:360-384.
13. Shuhaib M, Shah RA, Durrani I, Bilal. Electrokinetic viscous rotating disk flow of Poisson-Nernst-Planck equation for ion transport. J. Molecular Liquids. 2020;313:113412.
14. Bég OA, Rashid M, Mehr NF. Second law analysis of hydromagnetic flow from a stretching rotating disk: DTM-Padé simulation of novel nuclear MHD propulsion systems. Frontiers of

Aerospace Engineering. 2013;1:29-38.

15. Xun S, Zhao J, Zheng L, Chen X, Zhang X. Flow and heat transfer of Ostwald-de Waele fluid over a variable thickness rotating disk with index decreasing. Int. J. Heat Mass Transf. 2016;103:1214-1224.
16. Mishra SR, Shamshuddin M, Bég OA, Kadir A. Numerical study of heat transfer and viscous flow in a dual rotating extendable disk system with a non-Fourier heat flux model. Heat Transfer. 2019;48:435-459.
17. Zhang L, Anderson W, Zhang Z. Development and modeling of a rotating disc photocatalytic reactor for wastewater treatment. Chemical Engineering Journal, 2016;121: 125-134.
18. Rahman MA, Uddin MJ, Bég OA, Kadir A. Influence of variable viscosity and thermal conductivity, hydrodynamic, and thermal slips on magnetohydrodynamic micropolar flow: A numerical study. Heat Transfer Asian Res. 2019;1–17.
19. Khan WA, Khan M, Malik R. Three-dimensional flow of an Oldroyd-B nanofluid towards stretching surface with heat generation/absorption. Plos One. 2014;9:105107.
20. Khan M, Khan AZ, Alishomrani AS. Non-linear radiative flow of three-dimensional Burgers nanofluid with new mass flux effect. Int. J. of Heat and Mass Transfer. 2016;101:570–576.
21. Masood K, Khan. MHD boundary layer flow of a power-law nanofluid with new mass flux condition. AIP Advances. 2016;6:025211.
22. Khan M, Khan WA. Steady flow of Burger's nanofluid over a streatching surface with heat generation/absorption. J. Braz. Soc. Mech. Sci. Eng. 2016;38:2359-2367.
23. Khan WA, Irfan M, Khan M, Alshomrani AS. Impact of chemical processes on magneto nanoparticle for the generalized Burgers fluid. J. Mol. Liquids. 2017;234:201-208.
24. Khan WA, Alshomrani AS, Alzahrani AK, Khan M, Irfan M. Impact of autocatalysis chemical reaction on nonlinear radiative heat transfer of unsteady three-dimensional Eyring-Powell magneto-nanofluid flow. Pramana-J. Phys. 2018;91:63-72.
25. Bég, OA. Nonlinear multi-physical laminar nanofluid bioconvection flows: Models and computation. A. Sohail, Z. Li (Eds.): Computational Approaches in Biomedical Nano-Engineering, Chapter 5, 2018;113-145; Wiley.
26. Choi SUS. Enhancing thermal conductivity of fluids with nanoparticles, developments and

applications of non-Newtonian flows. American Society of Mechanical Engineers. J. Fluids Engineering. 1995;66:99-105.

27. Eastman JA, Choi SUS, Li S, Yu W, Thomson LJ. Anomalous increased effective thermal conductivities of ethylene glycol-based nanofluids containing copper nanoparticles. Appl. Phys. Lett. 2001;78:718-720.
28. Rana P, Bhargava R, Beg OA. Finite element simulation of unsteady MHD transport phenomena on a stretching sheet in a rotating nanofluid. Proc. IMECHE- Part N; J. Nanoengineering and Nanosystems. 2013;227:77-99.
29. Thumma T, Bég OA. Sheri SR. Finite element computation of transient dissipative double-diffusive magneto-convective nanofluid flow from a rotating vertical porous surface in porous media. Proc. IMechE- Part N– J. Nanoengineering Nanomaterials and Nanosystems. 2017;231:89–108.
30. Yadav D, Bhargava R, Agarwal GS, Hwang GS, Lee J, Kim MC. Magnetoconvection in a rotating layer of nanofluid. Asia Pacific Journal of Chemical Engineering. 2014;9:663-677.
31. Bachok N, Ishak A, Pop I. Flow and heat transfer over a rotating porous disk in a nanofluid. Phys B. 2011;406:1767–1772.
32. Mahanthesh B, Gireesha BJ, Shehzad, SA, Rauf A, Sampath Kumar PB. Nonlinear radiated MHD flow of nanoliquids due to a rotating disk with irregular heat source and heat flux condition. Physica B. 2018;537:98–104.
33. Makinde OD, Mahanthesh B, Gireesha BJ, Shashikumar NS, Monaledi RL, Tshehla MS. MHD nanofluid flow past a rotating disk with thermal radiation in the presence of aluminum and titanium alloy nanoparticles. Defect Diffus. Forum. 2018;384:69–79.
34. Sheikholeslami M, Hatami M, Ganji DD.Numerical investigation of nanofluid spraying on an inclined rotating disk for cooling process. J. Mol. Liq. 2015;211:577-583.
35. Hayat T, Imtiaz M, Alsaedi A, Alzahrani F. Effects of homogeneous-heterogeneous reactions in the flow of magnetite-Fe3O4 nanoparticles by a rotating disk. J. Mol. Liq. 2016;216:1214-1224.
36. Yin C, Zheng L, Zhang C, Zhang X. Flow and heat transfer of nanofluids over a rotating disk with uniform stretching rate in the radial direction. Propulsion Power Research. 2017; 6:25-30.

37. Mushtaq A, Mustafa M, Hayat T, Alsaedi A. Numerical study for rotating flow of nanofluids caused by an exponentially stretching sheet. Adv Powder Technol. 2016;27: 2223-2231.
38. Khan WA, Sultan F, Ali M, Shahzad M, Khan M, Irfan M. Consequences of activation energy and binary chemcial reaction for 3D flow of cross-nanofluid with radiative heat transfer. J. Braz. Soc. Mech. Sci. and Eng. 2019;41:4-17.
39. Khan WA, Ali M, Irfan M, Khan M, Shahzad M, Sultan F. A rheological analysis of nanofluid subjected to melting heat transport characteristics. Applied Nanoscience 2019. https://doi.org/10.1007/s13204-019-01067-5.
40. Khan WA, Ali M, Waqs M, Shahzad M, Sultan F, Irfan M, Importance of convective heat transfer in flow of non-Newtonian nanofluid featuring Brownian and thermophoretic diffusions. Int. J.of Numerical Methods for Heat and Fluid Flow. 2019;29:4624-4641.
41. Khan WA, Ali M, Shahzad M, Sultan F, Irfan M, Asghar Z. A note on activation energy and magnetic dipole aspects for cross nanofluid subjected to cylindrical surface. Applied Nanoscience. 2019. https://doi.org/10.1007/s13204-019-01220-0
42. Khan WA, Waqas M, Ali M, Sultan F, Shahzad M, Irfan M. Mathematical analysis of thermally radiative time dependent Sisko nanofluid flow for curved surface. Methods for Heat and Fluid Flow. 2019;29:3498-3514.
43. Khan WA, Waqas M, Chammam W, Asghar Z, Nisar UA, Abbas SZ. Evaluating the characteristics of magnetic dipole for shear-thinning Williamson nanofluid with thermal radiation. Computer Methods and Programs in Biomedicine. 2020. doi:https://doi.org/10.1016/j.cmpb.2020.105396.
44. Khan WA, Farooq S, Kadry S, Hanif M, Iftikhar FJ, Abbas SZ. Variable characteristics of viscosity and thermal conductivity in peristalsis of magneto-Carreau nanoliquid with heat transfer irreversibilities. Computer Methods and Programs in Biomedicine. (2020). https://doi.org/10.1016/j.cmpb.2020.105355
45. Khan WA, Khan MI, Kadry S, Farooq S, Khan MI, Abbas SZ. Transportation of water-based trapped bolus of SWCNTs and MWCNTs with entropy optimization in a non-uniform channel Neural Computing and Applications. 2020. https://doi.org/10.1007/s00521-020-04766-1.

46. Darcy HPC. Les Fontaines Publiques de la Ville de Dijon. Paris, France: Victor Dalmont; 1856.
47. Prasad V, Kulacki FA. Natural convection in porous media bounded by short concentric vertical cylinders. ASME J. Heat Transfer. 1985;107:147-154.
48. Vasseur P, Wang CH, Sen M. Natural convection in an inclined rectangular porous slot: Brinkman extended Darcy model. ASME J. Heat Transfer. 1990;112:507–511.
49. Umavathi JC, Kumar JP, Chamkha AJ, Pop I. Mixed convection in a vertical porous channel. Transp. Porous Media. 2005;61:315-335.
50. Umavathi JC, Patil MB, Pop I. On laminar mixed convection flow in a vertical porous stratum with symmetric wall heating conditions. Int. J. Trans. Phenom. 2006;8:127-140.
51. Umavathi JC, Kumar JP, Sultana J. Mixed convection flow in a vertical porous channel with boundary conditions of third kind with heat source/sink. J. Porous Media. 2012;15:998-1007.
52. Umavathi JC, Ravi Kanth ASV, Shekar M. Mixed convective flow in a vertical channel filled with porous medium using differential transform method. Int. J. Math. Arch. 2013;4:1-9.
53. Brinkman H.C. On the permeability of media consisting of closely-packed porous particles. Appl. Sci. Res. A. 1947;1:81-86.
54. Forchheimer P. Wasserbewegung durch Boden. Z. Ver. Deut. Ing. 1901;45: 1736-1741.
55. Umavathi JC, Bég OA. Numerical study of double-diffusive dissipative reactive convective flow in an open vertical duct containing a non-Darcy porous medium with Robin boundary conditions. J. Engineering Mathematics. 2019;119:135-147.
56. Rawat S, Bhargava, R, Bhargava R, Bég OA. Transient magneto-micropolar free convection heat and mass transfer through a non-Darcy porous medium channel with variable thermal conductivity and heat source effects. Proc. IMechE Part C- J. Mechanical Engineering Science. 2009;223:2341-2355.
57. Subba Rao A, Prasad VR, Bég OA, Rashidi M. Free convection heat and mass transfer of a nanofluid past a horizontal cylinder embedded in a non-Darcy porous medium. J. Porous Media. 2018;21:279-294.
58. Bég OA, Zueco J, Bég TA, Takhar HS, Kahya E. NSM analysis of time-dependent nonlinear buoyancy-driven double-diffusive radiative convection flow in non-Darcy geological porous media. Acta Mechanica. 2009;202:181-204.

59. Bég TA, Rashid M, Bég OA, Rahim N. Differential transform semi-numerical simulation of biofluid-particle suspension flow and heat transfer in non-Darcian porous media. Computer Methods Biomechanics Biomedical Engineering. 2013;16:896-907.
60. Bég OA, Uddin MJ, Bég TA, Kadir A, Shamshuddin M, Babaie M. Modeling mass transfer from a rotating cone in anisotropic porous media with Stefan blowing and Navier slip. Indian J.Physics. 2020;94:863-877.
61. Bég OA, Abdel Malleque K, Islam MN. Modeling of Ostwald-deWaele non-Newtonian flow over a rotating disk in a non-Darcian porous medium. Int. J. Applied Mathematics and Mechanics. 2012;8:46-67.
62. Prasad VR, SubbaRao, A, Bhaskar Reddy N, Vasu B, Bég OA. Modelling laminar transport phenomena in a Casson rheological fluid from a horizontal circular cylinder with partial slip. Proc. IMechE- Part E: J. Process Mechanical Engineering. 2013;227:309-326.
63. Mukhopadhyay S, Mandal IC. Magnetohydrodynamic (MHD) mixed convection slip flow and heat transfer over a vertical porous plate. Eng. Sci. Technol. Int. J. 2015;18:98-105.
64. Uddin MJ, Bég OA, Amin NS. Hydromagnetic transport phenomena from a stretching or shrinking nonlinear nanomaterial sheet with Navier slip and convective heating: a model for bio-nano-materials processing. J. Magnetism Magnetic Materials. 2014;368:252-261.
65. Bég OA, Faisal Md Basir M, Uddin MJ, Md. Ismail AI. Numerical study of slip effects on asymmetric bioconvective nanofluid flow in a porous microchannel with an expanding/contracting upper wall using Buongiorno's model. J. Mechanics in Medicine and Biology. 2017;17:1750059-1750086.
66. Shukla N, Rana P, Bég OA, Singh B, Kadir A. Homotopy study of magnetohydrodynamic mixed convection nanofluid multiple slip flow and heat transfer from a vertical cylinder with entropy generation. Propulsion and Power Research. 2019;8:147-162.
67. Prakash J, Tripathi D, Bég OA. Comparative study of hybrid nanofluid performance in microchannel slip flow induced by electroosmosis and peristalsis. Applied Nanoscience. 2020;10:1693-1706.
68. Shamshuddin M, Khan US, Bég OA, Bég TA. Hall current, viscous and Joule heating effects on steady radiative 3-D magneto-power-law polymer dynamics from an exponentially stretching sheet with power-law slip velocity: a numerical study. Thermal Science and

Engineering Progress. 2020:20, 100732.

69. Bég OA, Zueco J, López-Ochoa LM. Network numerical analysis of optically thick hydromagnetic slip flow from a porous spinning disk with radiation flux, variable thermophysical properties and surface injection effects. Chemical Engineering Communications. 2011;3:360-384.
70. Hayat T, Muhammad T, Shehzad SA, Alsaedi A. On magnetohydrodynamic flow of nanofluid due to rotating disk with slip effect: A numerical study. Comput. Methods Appl. Mech. Engrg. 2017;315:467-477.
71. Bég OA, Kabir N, Uddin MJ, Izani Md. Ismail A, Alginah A. Numerical investigation of Von Karman swirling bioconvective nanofluid transport from a rotating disk in a porous medium with Stefan blowing and anisotropic slip effects. Proc. IMechE- Part C- J. Mechanical Engineering Science. DOI: 10.1177/0954406220973061 (19 pages) 2020
72. Bég OA, Zohra FT, Uddin MJ, Ismail AIM, Satasivam. Energy conservation of nanofluids from a biomagnetic needle in the presence of Stefan blowing: Lie symmetry and numerical simulation. Case Studies in Thermal Engineering. 2021. https://doi.org/10.1016/j.csite.2021.100861.
73. Buongiorno J. Convective transport in nanofluids. ASME J. Heat Transfer. 2006;128: 240-250.
74. Uddin MJ, Bég OA, Ismail AI. Radiative-convective nanofluid flow past a stretching/shrinking sheet with slip effects. AIAA J. Thermophysics Heat Transfer. 2015;29: 513-523.
75. Russell, R.D., Christiansen, J., 1978. Adaptive mesh selection strategies for solving boundary value problems. SIAM J. Numer. Anal. 14, 59–80.
76. Bég, O.A., 2013. Numerical methods for multi-physical magnetohydrodynamics. J. Magnetohydrodynamics and Plasma Research. 18, 93-200.
77. Sarkar S, Sahoo B. Oblique stagnation flow towards a rotating disc. European Journal of Mechanics - B/Fluids. 2021;85:82-89.
78. Pal S. *Numerical Methods: Principles. Analyses and Algorithms*. Oxford University Press, India; 2009.
79. Jensen K, Einset E, Fotiadis D. Flow phenomena in chemical vapor deposition of thin films.

Annu. Rev. Fluid Mech. 1991;23:197-232.

80. Guha A, Sengupta S. Analysis of von Kármán's swirling flow on a rotating disc in Bingham fluids. Phys. Fluids. 2016;28:013601.